

**Crystalline Nickel Manganese Antimonate as a Stable Water-Oxidation Catalyst in
Aqueous 1.0 M H₂SO₄**

Ivan A. Moreno-Hernandez¹, Clara A. MacFarland¹, Carlos G. Read¹, Kimberly M.
Papadantonakis¹, Bruce S. Brunschwig², Nathan S. Lewis^{1,2,3}

¹Division of Chemistry and Chemical Engineering, 127-72, California Institute of Technology,
Pasadena, CA 91125, USA

²Beckman Institute Molecular Materials Research Center, California Institute of Technology,
Pasadena, CA 91125, USA

³Kavli Nanoscience Institute, California Institute of Technology, Pasadena, CA 91125, USA

*Correspondence to: nslewis@caltech.edu

Supplementary Information

Materials and Methods

Chemicals

All chemicals were used as received, including sulfuric acid (H_2SO_4 , Fisher Scientific, TraceMetal Grade, 93-98%), antimony(III) chloride (SbCl_3 , Alfa Aesar, ACS, 99.0% min), tin(IV) chloride hydrate ($\text{SnCl}_4 \cdot x\text{H}_2\text{O}$, Alfa Aesar, 98%), antimony standard for ICP (Sigma Aldrich, TraceCERT), multielement standard solution 1 for ICP (Sigma Aldrich, TraceCERT), potassium sulfate (K_2SO_4 , Macron Chemicals, ACS), and gallium-indium eutectic (Alfa Aesar, 99.99%). A Millipore deionized water system was used to obtain water with resistivity of 18.2 $\text{M}\Omega \text{ cm}$.

Sample Preparation

A conductive film of antimony-doped tin oxide (ATO) was deposited onto quartz slides via a spray pyrolysis procedure.¹ Briefly, the process consisted of heating a quartz slide at 550 °C on a hot plate, and using a spray gun to spray a 0.24 M ethanolic solution of SnCl_4 doped with 3 mol% SbCl_3 onto the quartz slide. The thickness of the ATO film was controlled by changing the duration of the spray. Films with a sheet resistance of 13-20 $\Omega \text{ sq}^{-1}$ were used for this study.

Sputter depositions were performed with an AJA Orion sputtering system. To make a direct contact to the ATO after film preparation, prior to depositing metal films the ATO-coated quartz slides were partially covered with Kapton tape. Multi-metal films were co-sputtered from three metal targets in an Ar plasma: Antimony (ACI Alloys, 99.95%), Nickel (ACI Alloys, 99.95%), and Manganese (ACI Alloys, 99.95%). An Ar flow rate of 20 sccm was used to sustain

the plasma, and the power applied to the three metal targets was varied to obtain films that had different compositions. The chamber pressure was 5 mTorr during the deposition, and the base pressure of the chamber was $< 10^{-7}$ Torr prior to use. The sample was not heated intentionally during the deposition process. The stoichiometry reported in the sample name was obtained by dissolving the deposited unannealed metal films in 1.0 M $\text{H}_2\text{SO}_4(\text{aq})$, followed by determination of the concentration of dissolved ions using ICP-MS.

After metal film deposition, the films were annealed in a muffle furnace (Thermolyne F48020-80) to form the oxides. The temperature was increased at a ramp rate of $10\text{ }^\circ\text{C min}^{-1}$ until the temperature set point was reached. The temperature was then held for 6 h and allowed to return to room temperature. The temperature set point was $700\text{ }^\circ\text{C}$ unless otherwise specified. Samples were cleaved into pieces, and In-Ga eutectic (Aldrich) was scribed on the ATO. Tinned Cu wire was threaded through a glass tube that had been cleaned with aqua regia, which consisted of a 3:1 v/v solution of concentrated hydrochloric acid and nitric acid, respectively. Ag paint (SPI, Inc.) was used to bond the wire to the portion of ATO that had been covered with In-Ga. The contact was allowed to dry for at least 2 h at room temperature or for 15 min at $85\text{ }^\circ\text{C}$ in an oven. Hysol 9460 epoxy was used to insulate the contact and define the electrode area, and the epoxy was allowed to cure for at least 12 h at room temperature. An optical scanner (Epson perfection V360) was used to image the electrode area and ImageJ was used to quantify the area. Electrode areas were between 1 and 11 mm^2 unless otherwise specified.

Materials Characterization

X-ray diffraction (XRD) analysis was performed with a Bruker D8 Discover instrument equipped with a 2-dimensional Vantec-500 detector. Copper $\text{K}\alpha$ radiation (1.54 \AA) was

generated with a tube voltage of 50 kV and a tube current of 1000 μ A. The incident beam was focused with a 0.5 mm diameter mono-capillary collimator. An aligned laser beam was used to ensure that the sample was placed at the correct depth for diffraction measurements. Coupled theta/two theta mode was used, with a θ angle that was half of the 2θ angle. The scattered x-ray radiation was collected by the Vantec-500 detector with an angular resolution $< 0.04^\circ$, which enabled the collection of diffraction from a 2θ range of 20° . Four scans were performed in the range of 25° to $85^\circ 2\theta$, and radiation was counted for a total duration of 4 h to obtain the XRD profile. The collected data were analyzed using Bruker EVA software. The peaks were indexed to reference patterns of SnO_2 and CoSb_2O_6 .^{2,3} The preferred orientation of the ATO crystals was not controlled during the ATO fabrication process, thus XRD data were not used for quantitative analysis. Transmission-electron microscopy (TEM) samples of the films were prepared using a focused Ga-ion beam (FIB) on a FEI Nova-600 Nanolab FIB/FESEM, with Pt and C protection layers being applied before being exposed to the FIB. High-resolution TEM (HRTEM) and scanning-transmission electron microscopy energy-dispersive X-ray spectroscopy (STEM-EDS) data were obtained using a Tecnai Polara (F30) TEM at an accelerating voltage of 300 keV.

X-ray Photoelectron Spectroscopy

X-ray photoelectron spectroscopy (XPS) data were collected using a Kratos Axis NOVA (Kratos Analytical, Manchester, UK) at a background pressure of 10^{-9} Torr. A monochromatic Al $K\alpha$ source at 1486.6 eV was used for excitation. Survey scans were collected at 1 eV resolution, whereas 0.05 eV resolution was used for high-resolution scans. The peak energies were calibrated against the binding energy of the adventitious C 1s peak, which was set at 284.8 eV.

The XPS $2p_{3/2}$ spectra of transition metal oxides are fit by multiple peaks, often 6, with the intensity of the individual peaks varying with the compound. Thus the energy for the intensity maximum of the observed spectra can significantly shift without a change in metal oxidation state. For example both NiO and Ni(OH)₂ are formally Ni(II) but the observed peak maxima differ by more than 1.5 eV.⁴ The Ni $2p_{3/2}$ spectra taken for Ni_{0.5}Mn_{0.5}Sb_{1.7}O_y before electrochemistry (Figure 4A) are similar to XPS spectra of Ni(OH)₂ and dissimilar to those of γ -NiOOH or β -NiOOH which have a maxima at ~ 856 eV.⁵ Also no sharp low energy peak for Ni metal was observed in Ni_{0.5}Mn_{0.5}Sb_{1.7}O_y (Figure 4A).⁵ The peak maximum observed for Ni(OH)₂ is ~ 855.3 eV compared to a maximum observed here of 855.3 eV.⁴ NiO has an observed maximum at 853.8 eV with a side peak at ~ 855.8 ,⁴ two peaks of almost equal height at 853.7 and 855.4 eV are used to fit these lines.⁶ The higher energy peak has an area of about 3 times that of the lower energy peak but the narrow width of the lower energy peak is responsible for the maximum in the observed spectra. Thus we assign the Ni in the Ni_{0.5}Mn_{0.5}Sb_{1.7}O_y compound to Ni(II). The Mn spectra taken before electrochemical operation qualitatively looked more like MnO than the higher oxides (Mn₂O₃, MnOOH, or MnO₂).⁵ The peak maximum observed here is 641.3 eV while that of MnO is ~ 641.5 eV. All the other Mn oxides have peak maxima close to 642 eV and have a sharp feature in the spectra at low energy. Thus we assign the Mn as Mn(II). The XP spectrum of Sb $3d_{5/2}$ overlaps with that of the O $1s$. The $3d_{3/2}$ XP spectra of the oxides of Sb shows peak maxima at 539.7 , 540.3 , and 540.6 eV for Sb₂O₃, Sb₂O₄, and Sb₂O₅, respectively.⁷ The Ni_{0.5}Mn_{0.5}Sb_{1.7}O_y had a $3d_{3/2}$ maxima at 539.7 eV and was assigned as Sb(III).

After electrochemical operation the Ni and Sb signals exhibited a shift towards higher binding energies by 0.39 and 0.33 eV, respectively.⁵ The shift of the Ni $2p_{3/2}$ maximum suggests

that Ni near the surface is partially oxidized.⁵ The surfaces of transition metal antimonates usually consist of a mixture of Sb^{3+} and Sb^{5+} . The observed 0.33 eV shift of the Sb $3d_{3/2}$ peak suggests that the surface Sb was oxidized, indicating that the surface changed from having a substantial Sb(III) component to adopting more Sb(V) character

Electrochemical Testing

Sulfuric acid (TraceMetal grade, Fisher Chemical) was used to make 1.0 M solutions, unless otherwise indicated. Digital potentiostats (SP-200, MPG-2, Bio-Logic Science Instruments) were used to acquire electrochemical data. Mercury/mercury sulfate electrodes (MSEs) were calibrated with a reversible hydrogen electrode (RHE). The RHE consisted of a platinum disk (CH Instruments) submerged in hydrogen-saturated 1.0 M sulfuric acid, with $\text{H}_2(\text{g})$ bubbled underneath the Pt disk. The potentials of the MSEs were between 0.676 V and 0.691 V vs. RHE. Glass electrochemical cells were cleaned with aqua regia prior to use. The working, reference, and counter electrodes consisted of the sample, a calibrated MSE, and a carbon rod (Strem) separated from the main compartment by a glass frit, respectively. Approximately 25 mL of 1.0 M $\text{H}_2\text{SO}_4(\text{aq})$ was used as the electrolyte, unless otherwise specified. The solution resistance was determined to be ~ 10 Ohm from impedance measurements on a platinum disk, and the electrochemical data were corrected for the solution resistance (i.e. 10 Ohm). Cyclic voltammetric data were collected at 10 mV s^{-1} unless otherwise specified.

The electrochemically active surface area (ECSA) was determined using a previously reported procedure.⁸ After cyclic voltammetry, the electrodes were held at open circuit for 1 min, and subsequently cyclic voltammetry scans were collected at $\pm 50 \text{ mV}$ from open circuit at scan rates of 100, 75, 25, and 10 mV s^{-1} . The current steps for the cyclic voltammetry were 100

μV and 100% of the current was acquired during each time step. The anodic and cathodic currents at the center of the cyclic voltammetry scans were plotted versus scan rate, and a linear fit was used to determine the capacitance. For all linear fits the R^2 value was greater than 0.99. Atomic-force microscopy was used to determine the roughness factor of the ATO ($\text{RF} = 1.32$), and the geometric area-normalized capacitance of ATO ($0.0254 \text{ mF cm}^{-2}$) was divided by the roughness factor to determine the capacitance normalized to the electrochemical surface area ($0.0192 \text{ mF cm}^{-2}$). The roughness factor for antimonates was calculated by dividing the electrochemical surface area determined by capacitance measurements by the geometric area of the electrode. Impedance measurements were performed in a static electrolyte of $1.0 \text{ M H}_2\text{SO}_4$ (aq) in the frequency range of $50 \text{ kHz} - 50 \text{ Hz}$. A potential of 1.63 V vs. RHE was applied and the amplitude of the sinusoidal wave amplitude was 10 mV .

Inductively-coupled plasma mass spectrometry

Inductively coupled plasma mass spectrometry (ICP-MS) data were collected using an Agilent 8800 Triple Quadrupole ICP-MS system. Calibration solutions were prepared by diluting the multielement and antimony standard solutions for ICP with $18.2 \text{ M}\Omega \text{ cm}$ resistivity water. To determine the loading of the catalysts, metal films were sputter deposited on glass slides and cut into $\sim 1 \text{ cm}^2$ pieces, and the geometric area of the pieces was measured with an optical scanner (Epson perfection V360) and ImageJ. The unannealed metal films on glass were placed in 10 mL of $1.0 \text{ M H}_2\text{SO}_4$ (aq), and the films were allowed to dissolve for several days. The total amount of Ni, Mn, and Sb in solution was determined from ICP-MS measurements, and the results were normalized to the geometric area of the pieces used.

A two-compartment electrolysis cell with a Nafion membrane separating the reference electrode and working electrode ($\sim 0.9 \text{ cm}^2$) from the counter electrode was used to determine the amount of Ni, Mn, and Sb from the working compartment (25 mL) in the electrolyte during chronopotentiometry at 10 mA cm^{-2} . At various time intervals 1 mL of electrolyte was taken from the working compartment, and immediately replenished with 1 mL of fresh electrolyte. The concentration of Ni, Mn, and Sb in the working compartment was determined for every time interval, and was corrected for the dilution that occurred each time a sample was taken.

Electrolyzer Efficiency Calculation and Solar Fuel Device Efficiency Discussion

The expected efficiency of an electrolyzer was calculated with equation 1. The overpotential for the hydrogen-evolution reaction (HER) was taken to be 80 mV (for example, Ni_2P and CoP),⁹ and the voltage drop from solution resistance was taken to be 100 mV. The efficiency for $\text{Ni}_{0.5}\text{Mn}_{0.5}\text{Sb}_{1.7}\text{O}_y$ ($\sim 745 \text{ mV}$ overpotential) was 57.7%, and for IrO_x ($\sim 350 \text{ mV}$) the efficiency was 69.9%.

The maximum efficiency expected when an optimized tandem cell is coupled with a set of electrocatalysts has been determined previously.¹⁰ Briefly, the procedure consists of determining the overall overpotential of the water splitting reaction, in this case 825 mV at 10 mA cm^{-2} (745 mV for $\text{Ni}_{0.5}\text{Mn}_{0.5}\text{Sb}_{1.7}\text{O}_y$ and 80 mV for an HER catalyst) and finding a combination of semiconductors operating at the Shockley-Queisser limit that maximize the efficiency of the device. For semiconductors operating at the Shockley-Queisser limit an efficiency above 20% can be obtained for devices with overall overpotentials and resistance losses $< 960 \text{ mV}$.¹⁰

$$Efficiency = \frac{1.229 V}{1.229 V + \eta_{OER} + \eta_{HER} + \eta_{iR}} \quad (1)$$

Turnover Frequency and Turnover Number Calculations

The turnover frequency and turnover number of $Ni_{0.5}Mn_{0.5}Sb_{1.7}O_y$ were determined by calculating the amount of catalyst with the total number of transition-metal atoms in the film or by estimating the number of exposed transition metals based on the electrochemically active surface area (ECSA). The ECSA should give an upper bound to the values, and the total number of transition metals should give a lower bound. An estimate for the surface atom density (4.6×10^{14} atoms cm^{-2}) based on the crystal structure of transition-metal antimonates was used to convert the ECSA to the number of transition-metal atoms exposed.

Supplementary Information Figures

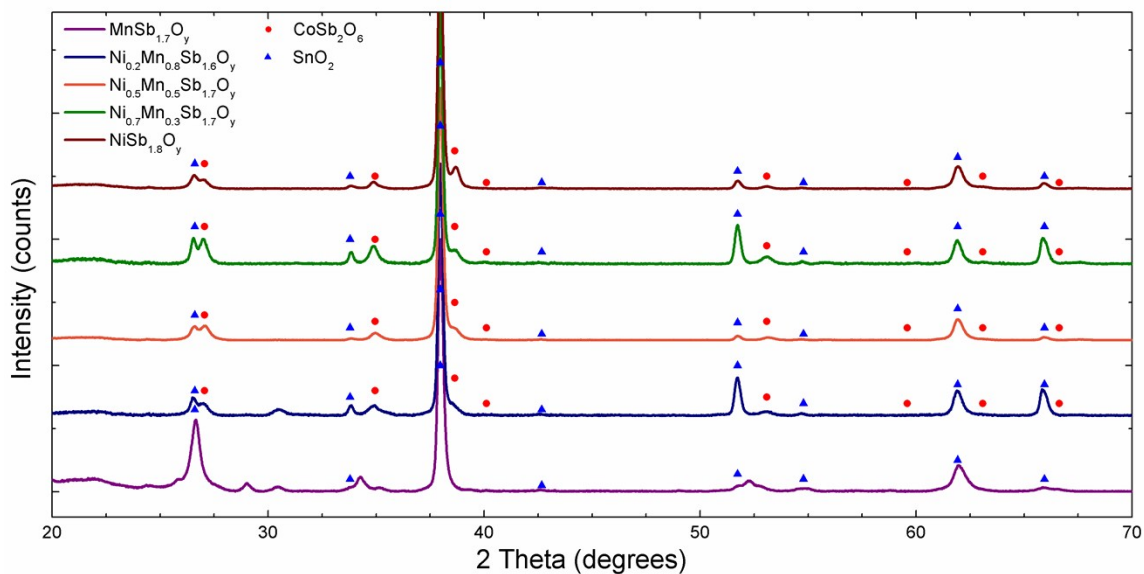


Figure S1. X-ray diffraction pattern for $\text{Ni}_x\text{Mn}_{1-x}\text{Sb}_{1.6-1.8}\text{O}_y$ thin films on an ATO substrate. The peaks were indexed to reference patterns of SnO_2 and CoSb_2O_6 .^{2,3}

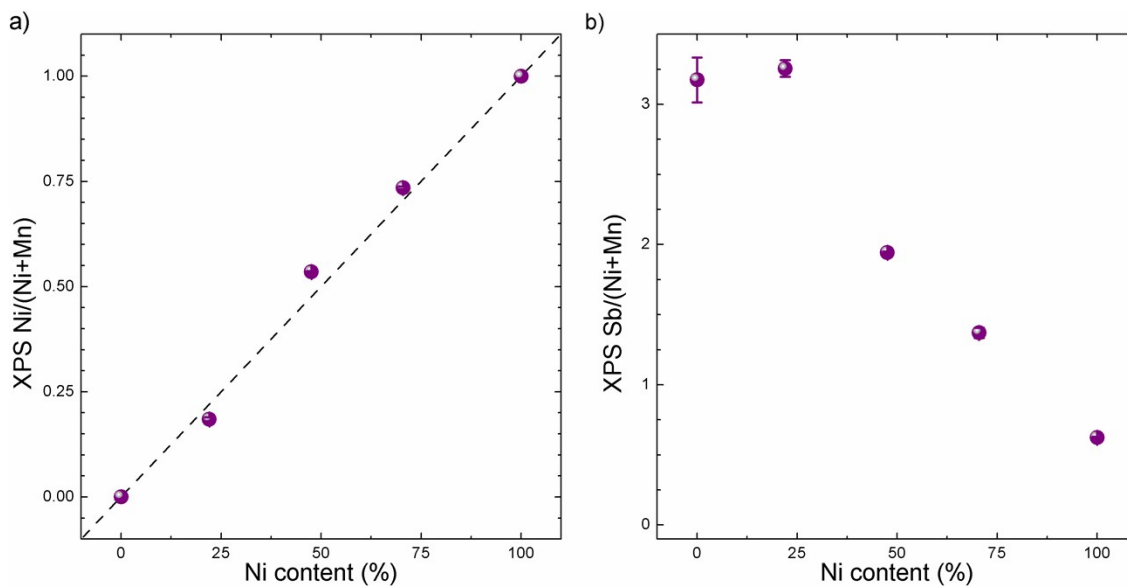


Figure S2. (a) Surface nickel-to-transition metal ratio and (b) surface antimony-to-transition metal ratio, as determined by XPS measurements, as a function of the bulk composition

determined by ICP-MS. Error bars are included in each data point and are one standard deviation from at least 3 samples.

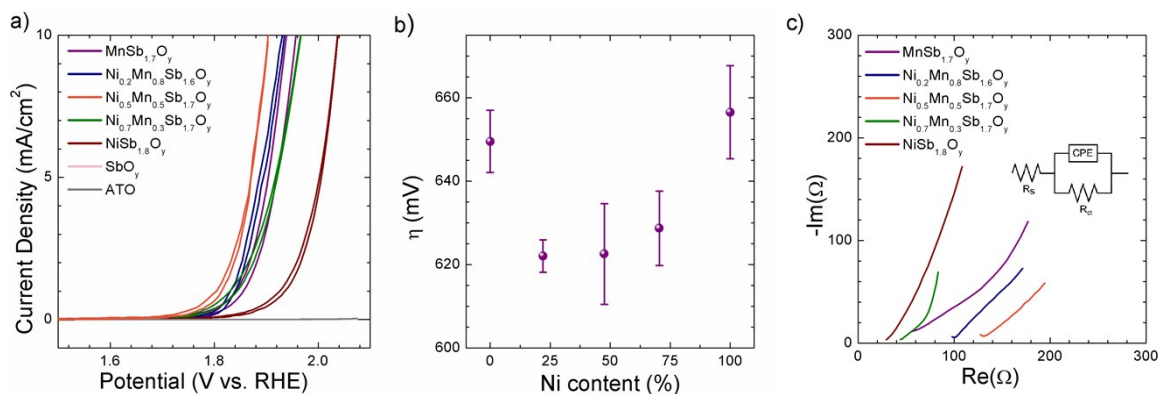


Figure S3. (a) Cyclic voltammetry of Ni_xMn_{1-x}Sb_{1.7}O_y, SbO_y, and ATO electrodes without resistance compensation. (b) Overpotential at 0.1 mA cm⁻² of electrochemically active surface area for Ni_xMn_{1-x}Sb_{1.7}O_y. (c) Impedance measurements of Ni_xMn_{1-x}Sb_{1.7}O_y, SbO_y in the frequency range of 50 Hz – 50 kHz, 10 mV amplitude in contact with 1.0 M H₂SO₄ (aq) at 1.63 V vs. RHE. Electrode areas were ~0.2 cm² for impedance measurements. Impedance data were fit to a model (insert) that consisted of the series resistance (R_s) associated with the electrode and electrolyte resistance, in series with a constant-phase element (CPE) in parallel with the contact resistance (R_{ct}) associated with the OER kinetics.

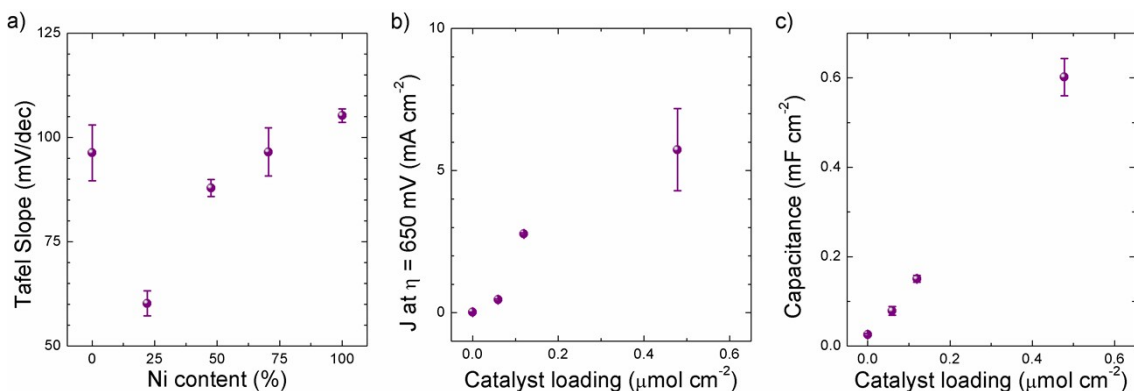


Figure S4. (a) Tafel slopes determined from cyclic voltammetry in the current density range of 0.3-3 mA cm⁻². (b) Current density (J) at $\eta = 650$ mV for Ni_{0.5}Mn_{0.5}Sb_{1.7}O_y at various loadings determined by calibration of the deposition rate of the sputterer. The loading is defined as the amount of Ni and Mn present in the as-synthesized film. A loading of 0.48 $\mu\text{mol cm}^{-2}$ corresponded to a film thickness of ~ 300 nm. Error bars are one standard deviation from at least 3 samples. (c) Area-normalized electrode differential capacitance at various loadings. Higher differential capacitance indicates more electrochemically active surface area.

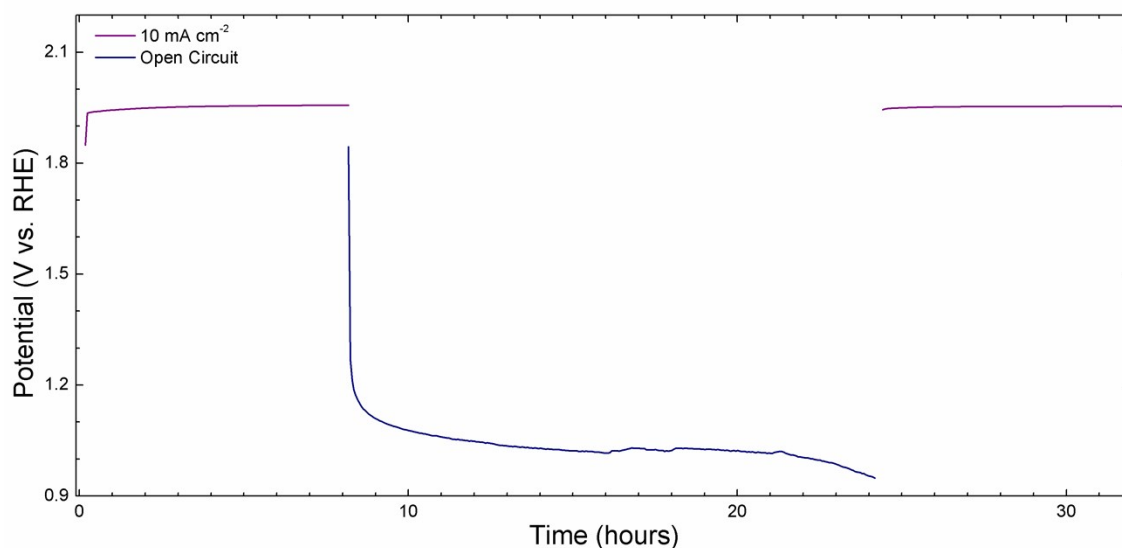


Figure S5. Potential of a Ni_{0.5}Mn_{0.5}Sb_{1.7}O_y electrode being held at 10 mA cm⁻² for 8 h, followed by 16 h at open circuit and subsequently being held at 10 mA cm⁻² for 8 h.

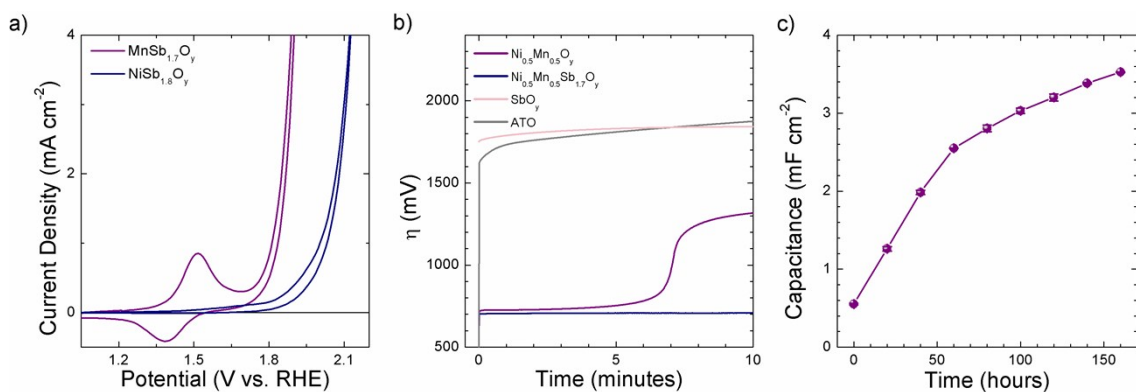


Figure S6. (a) Cyclic voltammetry of NiSb_{1.8}O_y and MnSb_{1.7}O_y after 50 h of chronopotentiometry at 10 mA cm⁻² based on the electrode geometric area. (b) Chronopotentiometry of Ni_{0.5}Mn_{0.5}O_y, SbO_y, ATO, and Ni_{0.5}Mn_{0.5}Sb_{1.7}O_y at 10 mA cm⁻² based on the electrode geometric area. (c) Area-normalized differential capacitance of a Ni_{0.5}Mn_{0.5}Sb_{1.7}O_y electrode determined between chronopotentiometry tests at 10 mA cm⁻² of geometric area.

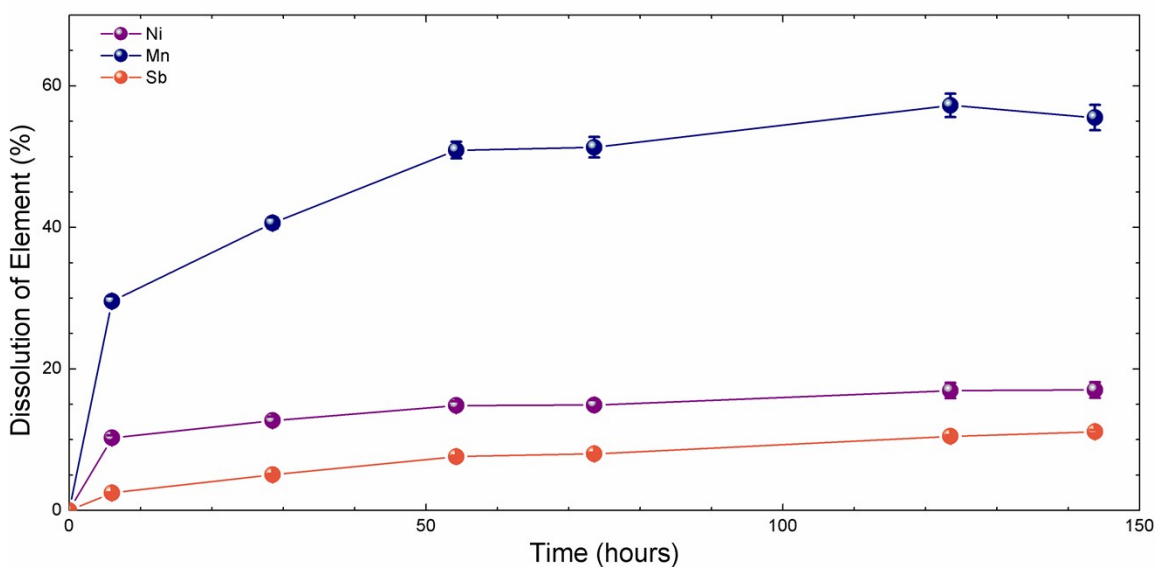


Figure S7. Cumulative dissolution of a Ni_{0.5}Mn_{0.5}Sb_{1.7}O_y electrode during chronopotentiometry at 10 mA cm⁻². The active electrode geometric area was 0.920 cm².

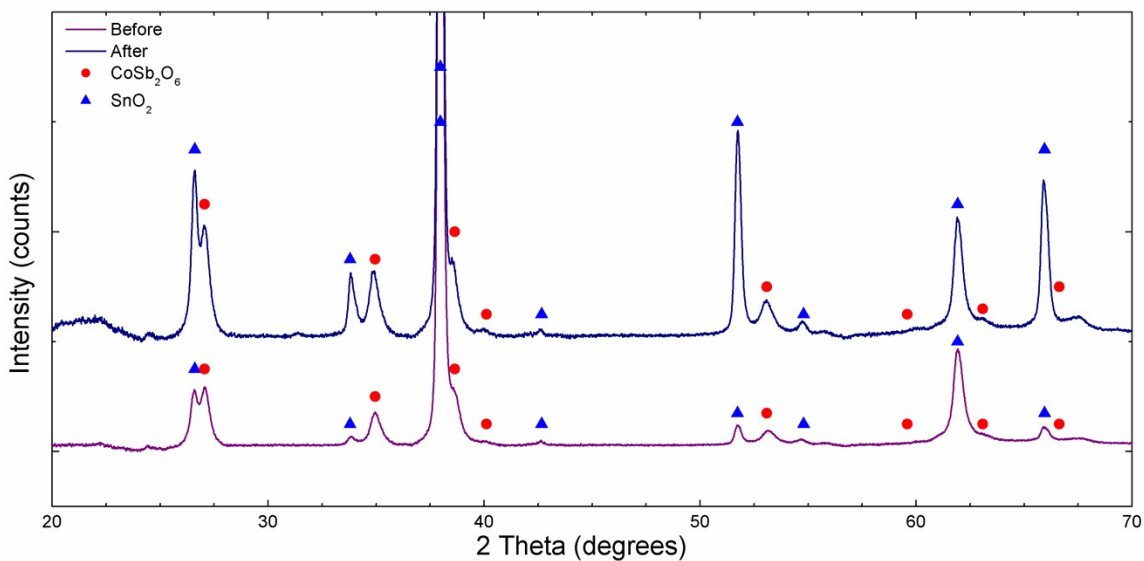


Figure S8. Diffraction pattern of $\text{Ni}_{0.5}\text{Mn}_{0.5}\text{Sb}_{1.7}\text{O}_y$ before and after chronopotentiometry for 144 h at 10 mA cm^{-2} of geometric area. The peaks were indexed to reference patterns of SnO_2 and CoSb_2O_6 .^{2,3}

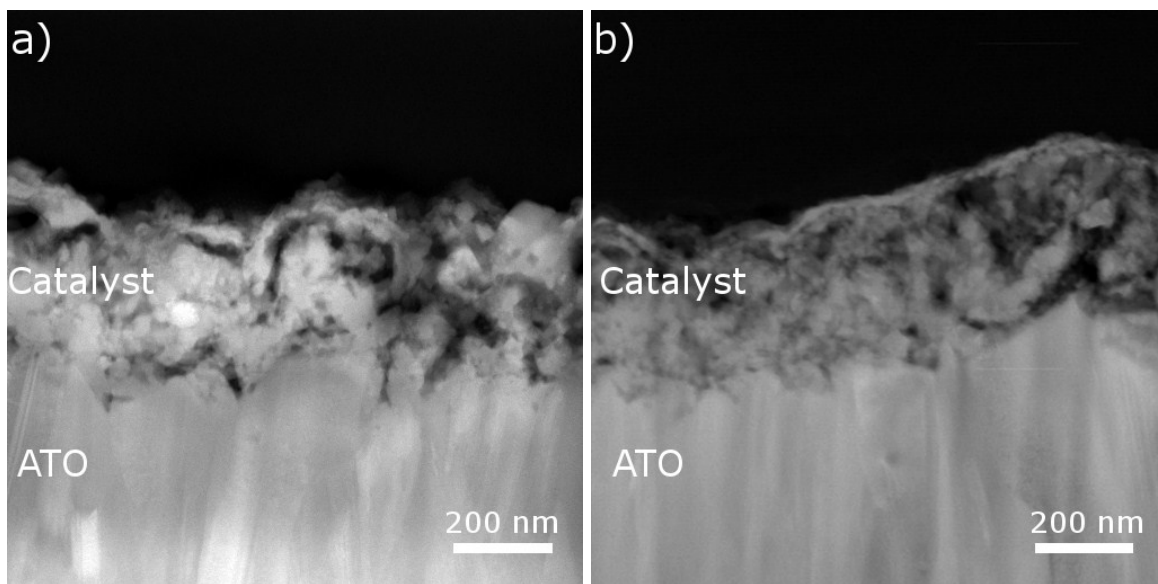


Figure S9. High-angle annular dark-field (HAADF) images of (a) $\text{Ni}_{0.5}\text{Mn}_{0.5}\text{Sb}_{1.7}\text{O}_y$ before electrochemical operation, and (b) $\text{Ni}_{0.5}\text{Mn}_{0.5}\text{Sb}_{1.7}\text{O}_y$ after chronopotentiometry for 144 h at 10 mA cm^{-2} . The lower portion of the image was identified as the ATO support, and a porous film

on top of the ATO was identified as the catalyst film. The film thickness for each image was measured as the distance between the compact ATO layer and the dark portion of the image corresponding to regions without material.

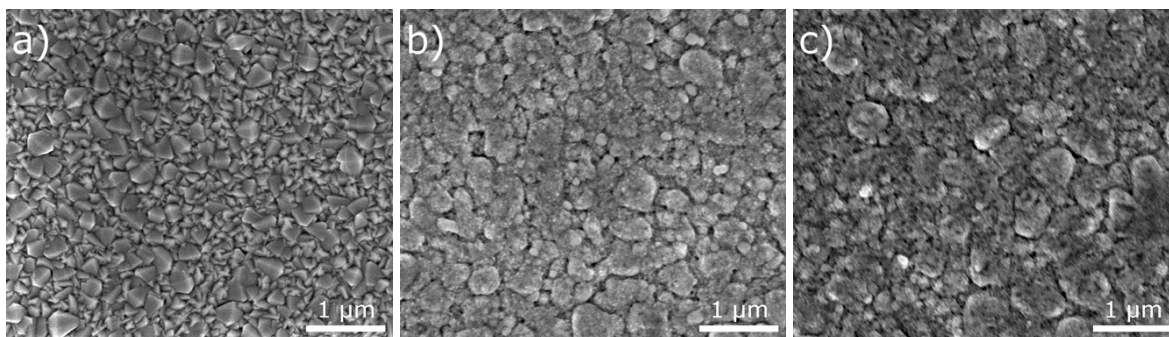


Figure S10. SEM images of (a) ATO substrate, (b) Ni_{0.5}Mn_{0.5}Sb_{1.7}O_y before electrochemical operation, and (c) Ni_{0.5}Mn_{0.5}Sb_{1.7}O_y after chronopotentiometry for 144 h at 10 mA cm⁻².

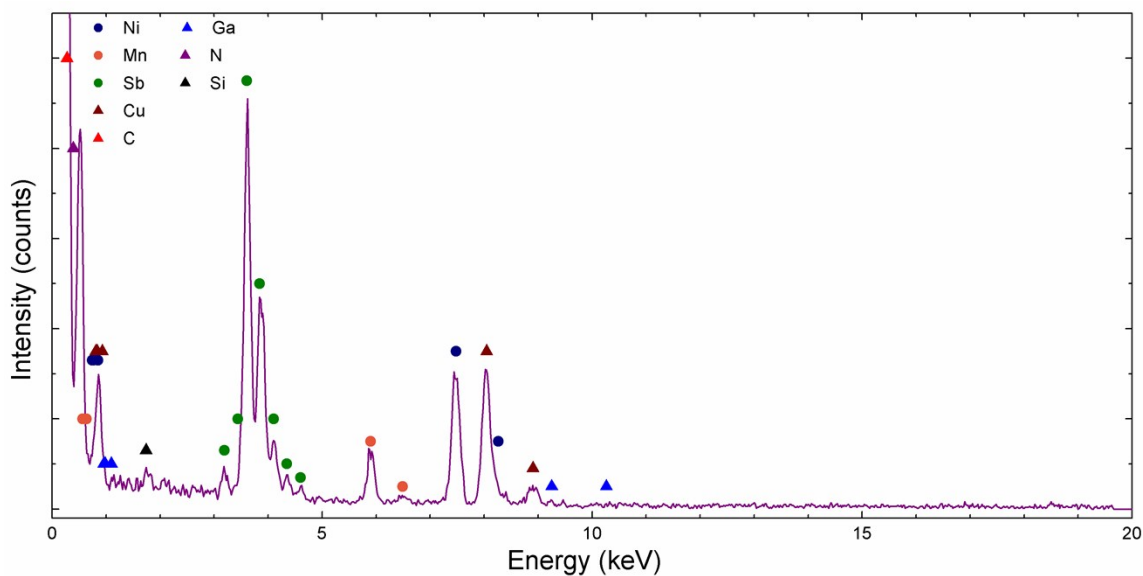


Figure S11. STEM-EDS data of as-synthesized Ni_{0.5}Mn_{0.5}Sb_{1.7}O_y showing that only Ni, Mn, Sb were detectable in the film. Cu, C, Ga, N, and Si are from the TEM grid and TEM sample preparation.

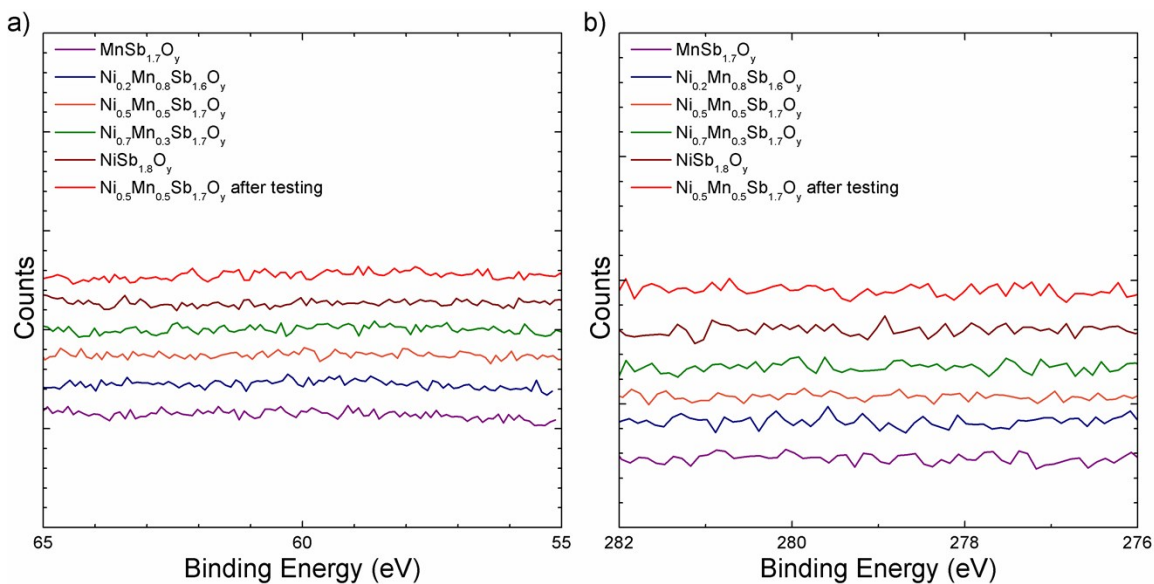


Figure S12. High-resolution XPS data of as-synthesized $\text{Ni}_x\text{Mn}_{1-x}\text{Sb}_{1.6-1.8}\text{O}_y$ and $\text{Ni}_{0.5}\text{Mn}_{0.5}\text{Sb}_{1.7}\text{O}_y$ after chronopotentiometry for 144 h at 10 mA cm^{-2} . The spectral regions are: (a) Ir 4f and (b) Ru 3d. No Ir or Ru was detected on the surface by XPS.

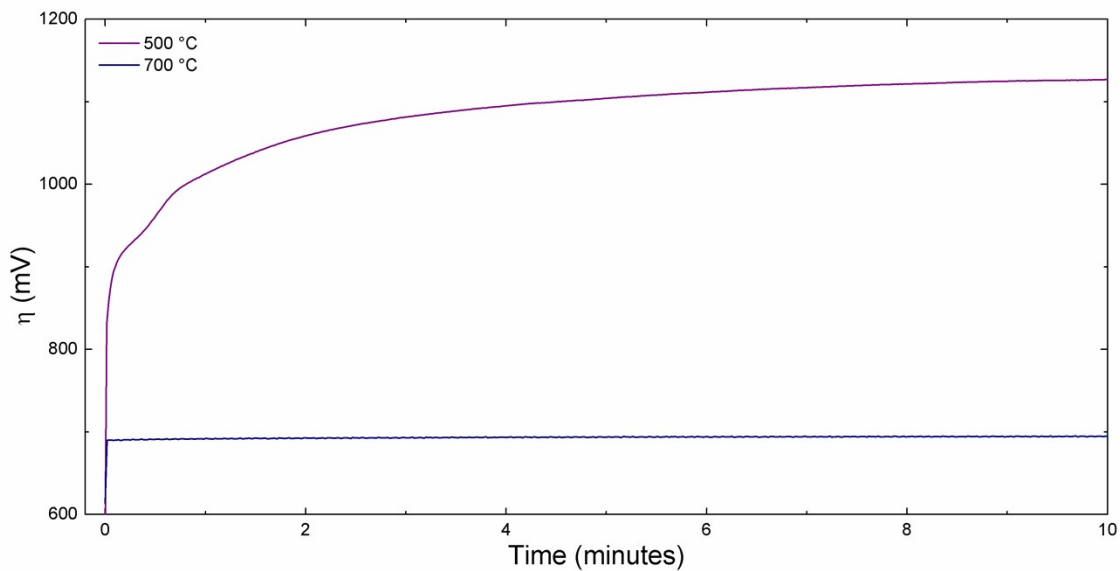


Figure S13. Chronopotentiometry at 10 mA cm^{-2} of $\text{Ni}_{0.5}\text{Mn}_{0.5}\text{Sb}_{1.7}\text{O}_y$ films annealed at $500 \text{ }^\circ\text{C}$ and $700 \text{ }^\circ\text{C}$.

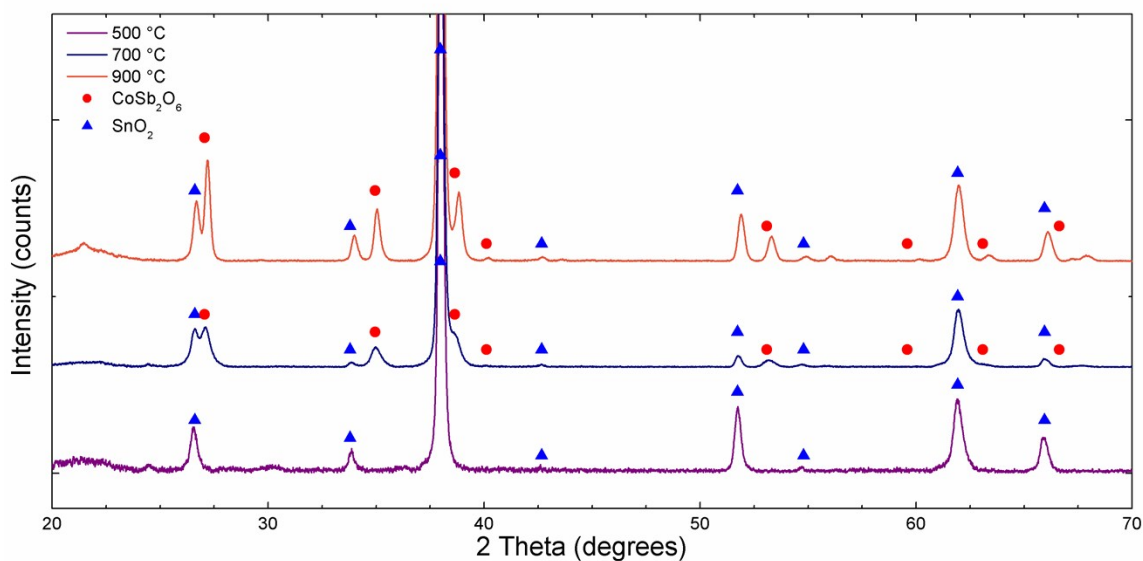


Figure S14. X-ray diffraction of $\text{Ni}_{0.5}\text{Mn}_{0.5}\text{Sb}_{1.7}\text{O}_y$ films annealed at 500 °C, 700 °C, and 900 °C. Reference patterns are SnO_2 (red circles) and CoSb_2O_6 (blue triangles).

Table S1. Composition of electrocatalysts determined with ICP-MS and initial roughness factor (RF) determined from capacitance measurements.

Sample	Ni ($\mu\text{mol cm}^{-2}$)	Mn ($\mu\text{mol cm}^{-2}$)	Sb ($\mu\text{mol cm}^{-2}$)	RF
$\text{MnSb}_{1.7}\text{O}_y$	0.000	0.475 ± 0.007	0.797 ± 0.005	18 ± 4
$\text{Ni}_{0.2}\text{Mn}_{0.8}\text{Sb}_{1.6}\text{O}_y$	0.111 ± 0.003	0.392 ± 0.005	0.808 ± 0.012	17 ± 2
$\text{Ni}_{0.5}\text{Mn}_{0.5}\text{Sb}_{1.7}\text{O}_y$	0.228 ± 0.004	0.251 ± 0.004	0.813 ± 0.008	29 ± 2
$\text{Ni}_{0.7}\text{Mn}_{0.3}\text{Sb}_{1.7}\text{O}_y$	0.342 ± 0.003	0.143 ± 0.002	0.819 ± 0.012	12 ± 1
$\text{NiSb}_{1.8}\text{O}_y$	0.470 ± 0.005	0.000	0.830 ± 0.003	4 ± 1

Table S2. Comparison of X-Ray Photoelectron spectroscopy peak positions for various samples.

Sample	Ni 2p _{3/2} (eV)	Mn 2p _{3/2} (eV)	Sb 3d _{3/2} (eV)	Reference
$\text{Ni}_{0.5}\text{Mn}_{0.5}\text{Sb}_{1.7}\text{O}_y$ Before	855.3 ± 0.1	641.3 ± 0.1	539.7 ± 0.1	
$\text{Ni}_{0.5}\text{Mn}_{0.5}\text{Sb}_{1.7}\text{O}_y$ After	855.6 ± 0.1	641.5 ± 0.1	540.0 ± 0.1	
$\text{Ni}(\text{OH})_2$	855.3 ± 0.1	-	-	4
NiO	853.8 ± 0.1	-	-	4
γ -NiOOH	856.2 ± 0.2	-	-	4
β -NiOOH	856.1 ± 0.1	-	-	4

MnO	-	641.5 ± 0.1	-	5
Sb ₂ O ₃	-	-	539.7 ± 0.1	7
Sb ₂ O ₄	-	-	540.3 ± 0.1	7
Sb ₂ O ₅	-	-	540.6 ± 0.1	7

References

1. H. Bisht, H.-T. Eun, A. Mehrkens and M. A. Aegerter, *Thin Solid Films*, 1999, **351**, 109-114.
2. W. H. Baur and A. A. Khan, *Acta Cryst.*, 1971, **B27**, 2133-2139.
3. J. N. Reimers, J. E. Greedan, C. V. Stager and R. Kremer, *J. Solid State Chem.*, 1989, **83**, 20-30.
4. A. P. Grosvenor, M. C. Biesinger, R. S. C. Smart and N. S. McIntyre, *Surf. Sci.*, 2006, **600**, 1771-1779.
5. M. C. Biesinger, B. P. Payne, A. P. Grosvenor, L. W. M. Lau, A. R. Gerson and R. S. C. Smart, *Appl. Surf. Sci.*, 2011, **257**, 2717-2730.
6. M. C. Biesinger, B. P. Payne, L. W. M. Lau, A. Gerson and R. S. C. Smart, *Surface and Interface Analysis*, 2009, **41**, 324-332.
7. R. Izquierdo, E. Sacher and A. Yelon, *Appl. Surf. Sci.*, 1989, **40**, 175-177.
8. C. C. McCrory, S. Jung, I. M. Ferrer, S. M. Chatman, J. C. Peters and T. F. Jaramillo, *J. Am. Chem. Soc.*, 2015, **137**, 4347-4357.
9. J. F. Callejas, C. G. Read, C. W. Roske, N. S. Lewis and R. E. Schaak, *Chemistry of Materials*, 2016, **28**, 6017-6044.
10. Y. Chen, S. Hu, C. Xiang and N. S. Lewis, *Energy Environ. Sci.*, 2015, **8**, 876-886.